Supplementary Materials 1 for

Arrhythmic hazard map for a 3D whole-ventricles model under multiple ion channel block

Jun-ichi Okada, Takashi Yoshinaga, Junko Kurokawa, Takumi Washio, Tetsushi Furukawa, Kohei Sawada, Seiryo Sugiura and Toshiaki Hisada

Correspondence to: okada@sml.k.u-tokyo.ac.jp

Supplementary Information

Supplementary Information

1. Extended Methods

1.1 *Geometry of the model*

We used a realistic model of the human heart embedded in a torso model based on a voxel-based, finite-element (FE) method. These models were used in our previous studies, and the details are described in those papers (Okada et al., 2011, 2015). The geometry of the model was based on multidetector computed tomography data of a subject without cardiac dysfunction collected with informed consent after approval of study by the institutional ethics committee.

Heart model: We analyzed only the ventricles, which consist of 244,187,136 voxel elements (mesh size 0.2 mm) (**SFig. 1.1A**). We mapped previously reported human data on the spatial orientation of the myocyte (fiber orientation) (http://gforge.icm.jhu.edu/gf/project/dtmri_data_sets) to this model of ventricles so the fiber orientation changed gradually from an endocardial to an epicardial surface [left ventricular (LV) free wall −90° to 60°; interventricular septum −90° to 70°, right ventricular (RV) free wall −60° to 60°] (**SFig. 1.1B**). Anisotropy of action potential propagation was introduced by setting the conductivity in the longitudinal (fiber) direction as greater than that in the transverse direction. To each voxel element, we implemented the ionic current model of human ventricular myocytes according to O'Hara et al. (O'Hara et al., 2011), which models three types of ventricular myocytes with different action potential durations (APDs)—i.e., endocardial cells, mid-myocardial (M-cells), and epicardial cells. We located M-cells in 20–64% of the wall volume from the endocardial side because we found that the physiological shape of T-waves could be reproduced with this distribution (Okada et al., 2011) (**SFig. 1.1C**). We modeled the conduction system, including the Purkinje system, using the network of one-dimensional elements with specific electrophysiological properties (Stewart et al., 2009) (**SFig. 1.1D**). Sites of the earliest activation (junctions of branches of bundles and the Purkinje network) were determined in our previous study (Okada et al., 2011) (**SFig. 1.1E**). With these settings we could reproduce the previously reported isochronal maps (Durrer et al., 1970) and body surface voltage maps (De Ambroggi et al., 1976; Taccardi, 1966).

Torso model: Mesh size of the voxel model of torso was 1.6 mm. We modeled major organs and applied specific conductivity to each of them (**SFig. 1.1F**; **STable 1.1).**

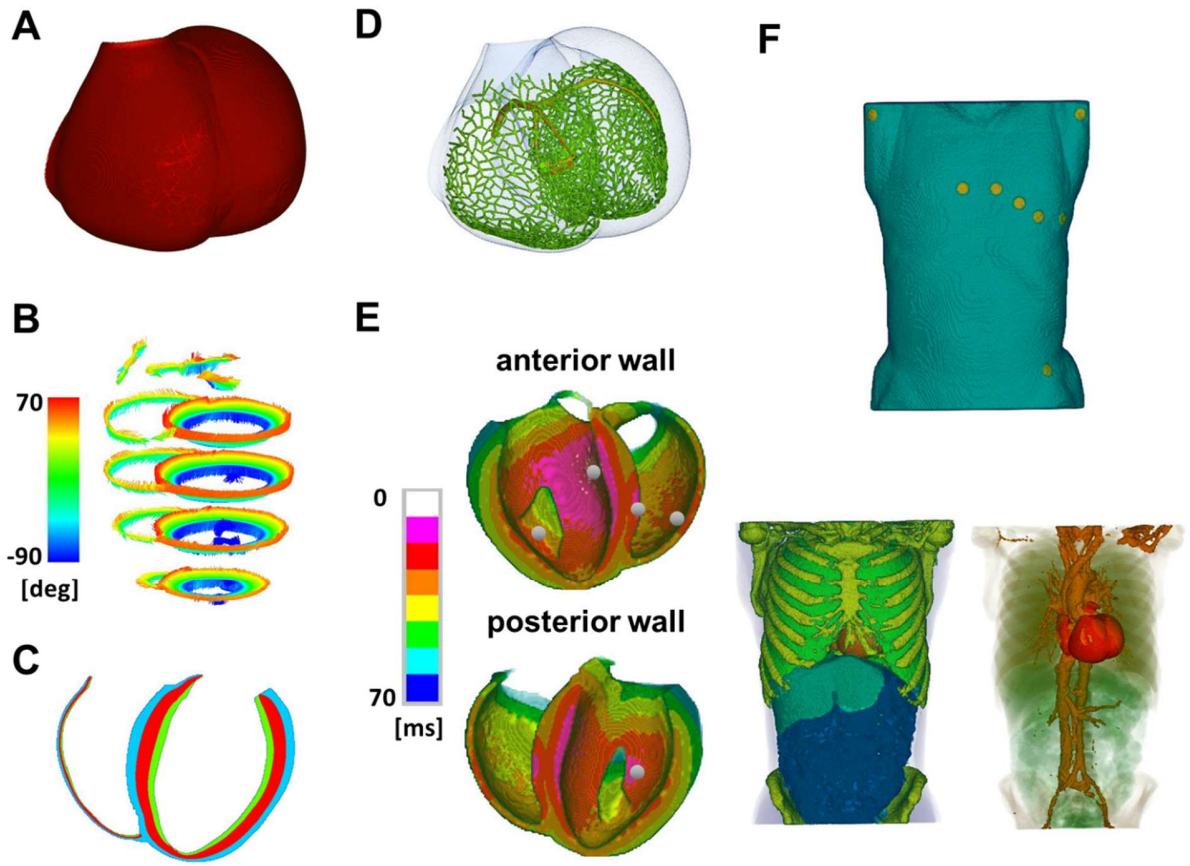

SFig. 1.1 Heart and torso models. A: Morphology of the ventricular model. **B:** Fiber orientation. Color indicates angles relative to the equatorial plane**. C:** Transmural distribution of endocardial cells (green), M-cells (red), and epicardial cells (blue). **D:** Conduction system. **E:** Earliest activation sites, where the Purkinje system is coupled to the myocardium (white dots), and activation sequences are seen from the anterior wall (*top panel*) and posterior wall (*bottom panel*). Color indicates the local activation time. **F:** Torso model: body surface with electrocardiographic electrodes (*top panel*) and major organs (*bottom panel*)

STable 1.1 Tissue conductivity

Ventricle (intracellular fiber direction)	6.2 [mS/cm] (Keldermann et al., 2009)	Ventricle (intracellular fiber normal direction)	2.0 [mS/cm] (Keldermann et al., 2009)
Ventricle (extracellular fiber direction)	4.0 [mS/cm] (Panescu, Webster, Tompkins & Stratbucker, 1995)	Ventricle (extracellular fiber normal direction)	2.0 [mS/cm] (Panescu, Webster, Tompkins & Stratbucker, 1995)
Blood	7.8[mS/cm] (Camacho, Lehr & Eisenberg, 1995)	Atrium	3.0 [mS/cm] (Panescu, Webster, Tompkins & Stratbucker, 1995)
Muscle	2.56 [mS/cm] (Panescu, Webster, Tompkins & Stratbucker, 1995)	Lung	0.83[mS/cm] (Panescu, Webster, Tompkins & Stratbucker, 1995)
Artery, vein	7.0 [mS/cm] (Panescu, Webster, Tompkins & Stratbucker, 1995)	Esophagus	2.0 [mS/cm] (Panescu, Webster, Tompkins & Stratbucker, 1995)
Stomach, bowel	2.0 [mS/cm] (Panescu, Webster, Tompkins & Stratbucker, 1995)	Lien, liver	1.67 [mS/cm] (Panescu, Webster, Tompkins & Stratbucker, 1995)
Bone	0.1 [mS/cm] (Camacho, Lehr & Eisenberg, 1995)	Kidney	1.67 [mS/cm] (Panescu, Webster, Tompkins & Stratbucker, 1995)
Fat	0.5 [mS/cm] (Panescu, Webster, Tompkins & Stratbucker, 1995)	Skin, body surface	40.0 [mS/cm] (model fit)

1.2 *Formulation of the propagation of excitation*

We defined three domains in the body (SFig. 1.2). The propagation of excitation in the body was formulated differently in these domains.

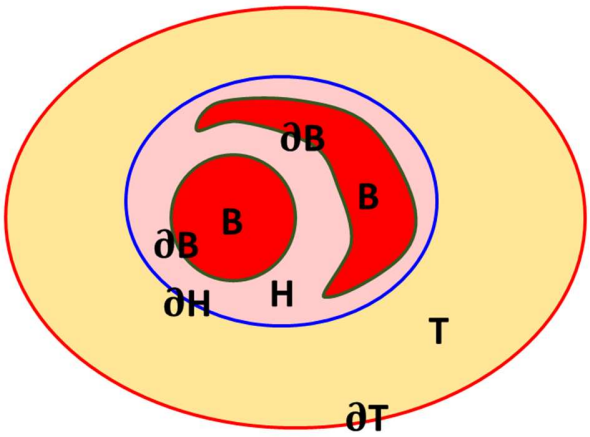

SFig. 1.2 Domains in the model. H: heart domain; B: blood domain; T: tissue domain. ∂H: boundary of heart domain; ∂B: boundary of blood domain; ∂T: boundary of tissue domain.

The excitable behavior of cardiac tissue (domain H) can be modeled as a continuous system using the following bi-domain equations:

$$\beta\left(C_m\frac{\partial V_m}{\partial t}+I_{ion}\right)=-I_{stim}+\frac{\partial}{\partial x_i}\left(G_{ij}^{I}\frac{\partial \emptyset^{I}}{\partial x_j}\right),\qquad in\ H, \tag{S1}$$

$$\beta\left(C_m\frac{\partial V_m}{\partial t}+I_{ion}\right)=I_{stim}-\frac{\partial}{\partial x_i}\left(G_{ij}^{E}\frac{\partial \emptyset^{E}}{\partial x_j}\right),\qquad in\ H, \tag{S2}$$

where $\emptyset^{I}$ and $\emptyset^{E}$ are the intracellular and extracellular potentials, respectively; $V_m=\emptyset^{I}-\emptyset^{E}$ is the transmembrane voltage; β is the surface-to-volume ratio of the tissue (= 2000 cm^{-1}) (Ten Tusscher et al., 2004); Cm is membrane capacitance (= 1 $\mu F/cm^2$) (O'Hara et al., 2011); t is time; G_{ij}^{I} and G_{ij}^{E} are the extracellular and intracellular conductivity tensors, respectively, accounting for the anisotropy of cardiac tissue; I_{stim} is the stimulation current; I_{ion} is the sum of ionic transmembrane currents describing the excitable behavior of individual ventricular cells; and indices *i* and *j* vary from 1 to 3. In the torso (T) and blood (B) domains, Laplace's equation was solved.

$$\frac{\partial}{\partial x_i}\left(G_{ij}^{T}\frac{\partial \emptyset^{T}}{\partial x_i}\right)=0, \qquad in\ T, \tag{S3}$$

$$\frac{\partial}{\partial x_i}\left(G_{ij}^{B}\frac{\partial \emptyset^{B}}{\partial x_i}\right)=0, \qquad in\ B, \tag{S4}$$

where $\emptyset^{T}, \emptyset^{B}$ is the potential; G_{ij}^{T}, G_{ij}^{B} is the isotropic conductivity at each point. In the torso domain, we assigned distinct values of G_{ij}^{T} for each organ adopted from the literature. On the boundaries of each domain, the following conditions were imposed, including the electrical coupling between the extracellular space of the heart domain and the torso domain (∂H) or the blood domain (∂B).

$$n_i\left(G_{ij}^{T}\frac{\partial \emptyset^{T}}{\partial x_j}\right)=0, \qquad on\ \partial T, \tag{S5}$$

$$n_i\left(G_{ij}^{I}\frac{\partial \emptyset^{I}}{\partial x_j}\right)=0, \qquad on\ \partial H, \tag{S6}$$

$$n_i\left(G_{ij}^{E}\frac{\partial \emptyset^{E}}{\partial x_j}\right)=n_i\left(G_{ij}^{T}\frac{\partial \emptyset^{T}}{\partial x_j}\right), \qquad \emptyset^{E}=\emptyset^{T},\ on\ \partial H, \tag{S7}$$

$$n_i\left(G_{ij}^{E}\frac{\partial \emptyset^{E}}{\partial x_j}\right)=n_i\left(G_{ij}^{B}\frac{\partial \emptyset^{B}}{\partial x_j}\right), \qquad \emptyset^{E}=\emptyset^{B},\ on\ \partial B, \tag{S8}$$

Conductivities are listed in STable 1.1.

1.3 *FE element discretization*

By applying the divergence theorem to the weak form of equations (S1) and (S2), we obtain

$$\begin{aligned}\int_H \delta\emptyset^{I}\beta\left(C_m\frac{\partial V_m}{\partial t}+I_{ion}\right)dV \\ =-\int_H G_{ij}^{I}\frac{\partial\delta\emptyset^{I}}{\partial x_i}\frac{\partial\emptyset^{I}}{\partial x_j}dV+\int_{\delta H}\delta\emptyset^{I}n_iG_{ij}^{I}\frac{\partial\emptyset^{I}}{\partial x_j}dS,\end{aligned} \tag{S9}$$

$$\begin{aligned}\int_H \delta\emptyset^{E}\beta\left(C_m\frac{\partial V_m}{\partial t}+I_{ion}\right)dV \\ =\int_H G_{ij}^{E}\frac{\partial\delta\emptyset^{E}}{\partial x_i}\frac{\partial\emptyset^{E}}{\partial x_j}dV-\int_{\delta H}\delta\emptyset^{E}n_iG_{ij}^{E}\frac{\partial\emptyset^{E}}{\partial x_j}dS.\end{aligned} \tag{S10}$$

Note the second terms of the right-hand side of (S9) becomes zero from (S6). The FE discretization of (S9) and (S10) using

$$\begin{aligned} V_m &= N_a V_{m,a}, \qquad \delta V_m = N_a \delta V_{m,a}, \\ \emptyset^I &= N_a \emptyset_{I,a}, \qquad \delta\emptyset^I = N_a \delta\emptyset_{I,a}, \\ \emptyset^E &= N_a \emptyset_{E,a}, \qquad \delta\emptyset^E = N_a \delta\emptyset_{E,a}, \end{aligned} \tag{S11}$$

leads to the following matrix representation.

$$\beta\{I_m\} = -[K_I]\{\emptyset_I\}, \tag{S11}$$

$$\beta\{I_m\} = -\{F_E\} + [K_E]\{\emptyset_E\}, \tag{S12}$$

where

$$\{I_m\} = \int_H N_a I_{ion} dV + [C]\left\{\frac{\partial V_m}{\partial t}\right\}, \qquad [C] = \int_H N_a C_m N_b dV,$$

$$[K_I] = \int_H \frac{\partial N_a}{\partial x_i} G_{ij}^I \frac{\partial N_b}{\partial x_j} dV, \qquad [K_E] = \int_H \frac{\partial N_a}{\partial x_i} G_{ij}^E \frac{\partial N_b}{\partial x_j} dV,$$

$$\{F_E\} = \int_{\delta H} \delta\emptyset^E n_i G_{ij}^E \frac{\partial \emptyset^E}{\partial x_j} dS.$$

By subtracting (S12) from (S11) and with the relation $\{V_m\} = \{\emptyset_I\} - \{\emptyset_E\}$, we obtain

$$\left[[K_I] + [K_E]\right]\{\emptyset_E\} = \{F_E\} - [K_I]\{V_m\}, \tag{S13}$$

Equations (S3) and (S4) are discretized similarly to give

$$[K_T]\{\emptyset_T\} = \{F_T\}, \tag{S14}$$

$$[K_B]\{\emptyset_B\} = \{F_B\}, \tag{S15}$$

where

$$[K_T] = \int_T \frac{\partial N_a}{\partial x_i} G_{ij}^T \frac{\partial N_b}{\partial x_j} dV, \qquad [K_B] = \int_B \frac{\partial N_a}{\partial x_i} G_{ij}^B \frac{\partial N_b}{\partial x_j} dV,$$

$$\{F_T\} = \int_{\delta T} \delta\emptyset^T n_i G_{ij}^T \frac{\partial \emptyset^T}{\partial x_j} dS + \int_{\delta H} \delta\emptyset^T n_i G_{ij}^T \frac{\partial \emptyset^T}{\partial x_j} dS,$$

$$\{F_B\} = \int_{\delta B} \delta\emptyset^B n_i G_{ij}^B \frac{\partial \emptyset^B}{\partial x_j} dS.$$

From (S5), (S7), and (S8), the fluxes and potentials on each boundary satisfy the following conditions.

$$\{F_E\} = \{F_T\}, \qquad \{\emptyset_E\} = \{\emptyset_T\}, \qquad on\ \partial H, \tag{S16}$$

$$\{F_E\} = \{F_B\}, \qquad \{\emptyset_E\} = \{\emptyset_B\}, \qquad on\ \partial B, \tag{S17}$$

$$\{F_T\} = 0, \qquad on\ \partial T. \tag{S18}$$

With the FE method, the continuity of the potential and the conservation of nodal current are satisfied by sharing the degrees of freedom on the boundary. Finally, the matrix form describing the whole system can be obtained as

$$\begin{bmatrix} [K_I]+[K_E] & [K_I]+[K_E] & [K_I]+[K_E] & 0 & 0 \\ [K_I]+[K_E] & [K_I]+[K_E]+[K_T] & 0 & [K_T] & 0 \\ [K_I]+[K_E] & 0 & [K_I]+[K_E].+[K_B] & 0 & [K_B] \\ 0 & [K_T] & 0 & [K_T] & 0 \\ 0 & 0 & [K_B] & 0 & [K_B] \end{bmatrix} \begin{Bmatrix} \emptyset_{E\ in\ H} \\ \emptyset_{E,T\ on\ \partial H} \\ \emptyset_{E,B\ on\ \partial B} \\ \emptyset_{T\ in\ T} \\ \emptyset_{B\ in\ B} \end{Bmatrix} = \begin{Bmatrix} -[K_I]\{V_m\} \\ -[K_I]\{V_m\} \\ -[K_I]\{V_m\} \\ 0 \\ 0 \end{Bmatrix} \tag{S19}$$

The algorithm for time evolution is shown in SFig.1.3. Time steps used for the calculation of excitation propagation were 0.01 and 1.0 ms for the ECG calculation. Model parameters and the definition of the model are summarized in STable 1.2 and STable 1.3, respectively.

Set initial value

Compute : $[K_I], [K_E], [K_T], [K_B], [\mathrm{C}]^{-1}$

For k = 1,……k_{end}

$$T = t_0 + (k-1)\Delta\mathrm{T}$$

Solve:
$$\begin{bmatrix} [K_I]+[K_E] & [K_I]+[K_E] & [K_I]+[K_E] & 0 & 0 \\ [K_I]+[K_E] & [K_I]+[K_E]+[K_T] & 0 & [K_T] & 0 \\ [K_I]+[K_E] & 0 & [K_I]+[K_E]+[K_B] & 0 & [K_B] \\ 0 & [K_T] & 0 & [K_T] & 0 \\ 0 & 0 & [K_B] & 0 & [K_B] \end{bmatrix} \begin{Bmatrix} \emptyset_{E\ in\ H} \\ \emptyset_{E,T\ on\ \partial H} \\ \emptyset_{E,B\ on\ \partial B} \\ \emptyset_{T\ in\ T} \\ \emptyset_{B\ in\ B} \end{Bmatrix} = \begin{Bmatrix} -[K_I]\{V_m\} \\ -[K_I]\{V_m\} \\ -[K_I]\{V_m\} \\ 0 \\ 0 \end{Bmatrix}$$

For i = 1,……$\Delta T\ /\Delta t$

$$t = (i-1)\Delta t + T$$

$$\{\emptyset_I^t\} = \{\emptyset_E^T\} + \{V_m^t\}$$

Compute : $\{I_{ion}(V_m^t)\}$

$$\{V_m^{t+\Delta t}\} = \Delta t[\mathrm{C}]^{-1}\left\{-\frac{[K_I]\{\emptyset_I^t\}}{\beta} - \{I_{ion}\}\right\} + \{V_m^t\}$$

next i

next k

ΔT : Time step for ECG calculation

Δt : Time step for excitation propagation

SFig. 1.3 Algorithm for calculating the propagation of excitation and ECG

STable 1.2 Model parameters

Parameters	Values
Element type	Eight-node hexahedral elements
Time step for ECG calculation [ms]	1.0
Time step for excitation propagation [ms]	0.01
Mesh size of heart region [cm]	0.02
Mesh size of torso region [cm]	0.16
Fiber orientation	From endocardial to epicardial surface: -90° to 60° in LV free wall -90° to 70° in ventricular septum -60° to 60° in RV free wall
Transmural distribution of cell types (endothelial/M/epithelial) [volume ratio]	20:44:36
β (surface area-to-volume ratio) [cm^{-1}]	2000
C_m (membrane capacitance) [$\mu\mathrm{F/cm}^2$]	1

STable 1.3 Definition of the model

Variable	Description
Equations	Bi-domain
Material	Transversely isotropic
PDE solver	Fully explicit
Cell model variant	O'Hara et al. (2011)
Cell model numerical integration scheme	Explicit
Mesh type	Hexahedral
Solution method	Finite element
Basis function	Bi-linear
Pre-conditioners	Incomplete LU
Matrix solver	Generalized minimal residual
System architecture	Distributed memory

PDE: partial differential equation; LU: Lower-Upper

1.1 *In vitro* current assay

Ion currents were recorded in CHO or CHL cells expressing either hERG (I_{Kr}), Nav1.5, (I_{Na}), Cav1.2/b2/a2-d (I_{Ca}), KCNQ1+KCNE1 (I_{Ks}) channels using the Sophion QPatch HTX system and software (QPatch Assay Software 5.0; Biolin Scientific, Stockholm, Sweden) using the following cell lines, assay buffers, and voltage protocols.

Cell lines: hERG (KCNH2 gene) channels were stably expressed in CHO-K1 cells. Nav1.5 (SCN5A gene, hNav1.5 channel) channels were stably expressed in CHL cells. Cav1.2 (CACNA1C/CACNB2/CACNA2D1 genes) channels were stably expressed in CHO cells. Iks (KCNQ1/KCNE1 genes) channels were stably expressed in CHO-K1 cells. hERG, Nav1.5 and Iks Ik1 cell lines were established in Eisai. The Cav1.2 cell line was purchased from ChanTest Corporation (Cleveland, OH, USA).

Assay buffers: I_{Kr}: extracellular solution and internal solution containing (in mM): 145 NaCl, 4 KCl, 2 $CaCl_2$, 1 $MgCl_2$, 10 HEPES, 10 glucose, pH adjusted to 7.4 with NaOH, and 120 KCl, 5 $CaCl_2$, 1.8 $MgCl_2$, 10 KOH/EGTA, 4 Na2-ATP, 10 HEPES, pH adjusted to 7.2 with KOH. I_{Na}: extracellular solution and internal solution containing (in mM): 145 NaCl, 4 KCl, 2 $CaCl_2$, 1 $MgCl_2$, 10 HEPES, 10 glucose, pH adjusted to 7.4 with NaOH, and 135 CsF, 10 NaCl, 1 EGTA, 10 HEPES, pH adjusted to 7.3 with CsOH. I_{Ca}: extracellular solution and internal solution containing (in mM): 137 NaCl, 4 KCl, 1.8 $CaCl_2$, 1 $MgCl_2$, 10 HEPES, 10 glucose, pH adjusted to 7.4 with NaOH, and 80 L-aspartic acid, 130 CsOH, 5 $MgCl_2$, 4 Na2-ATP, 0.1 Tris-GTP, 5 EGTA, 10 HEPES, pH adjusted to 7.2 with L-aspartic acid. I_{Ks}: extracellular solution and internal solution containing (in mM): 145 NaCl, 4 KCl, 2 $CaCl_2$, 1 $MgCl_2$, 10 HEPES, 10 glucose, pH adjusted to 7.4 with NaOH, and 110 K-gluconate, 20 KCl, 2 $MgCl_2$, 5 EGTA, 4 Na2-ATP, 10 HEPES, pH adjusted to 7.2 with KOH.

Voltage protocols: I_{Kr} was induced by the application of depolarizing step pulses to +20 mV with 2000 ms duration, followed by step pulses to -50 mV with 2000 ms duration from a holding potential of -80 mV every 15 s. The inhibition ratio of the tail current at -50 mV was calculated as hERG inhibition. I_{Na} was induced by the application of 30 repetitive depolarizing pulses to -10 mV with 50 ms duration from a holding potential of -90 mV at 2 Hz. The inhibition ratio of peak inward current at the 30^{th} pulse was calculated as I_{Na} inhibition. I_{ca} was induced by the application of depolarizing step

pulses to 0 mV with 150 ms duration from a holding potential of -40 mV every 5 s. The inhibition ratio of peak inward current was calculated as I_{Ca} inhibition. I_{ks} was induced by the application of depolarizing step pulses to +40 mV with 2000 ms, followed by step pulses to -50 mV with 500 ms duration from the holding potential of -80 mV every 5 s. The inhibition ratio of tail current at -50 mV was calculated as I_{Ks} inhibition.

Starting from the free effective therapeutic plasma concentration ($ETPC_{unbound}$), drug concentrations were increased until the inhibition rate of any one of five currents reached its upper limit or arrhythmias were observed. Drug effects were analyzed for each channel by normalizing the current by its maximum value obtained in the absence of the drug and fit to the Hill equation, where x and h represent the drug concentration and Hill constant, respectively.

$$\text{Relative current} = \frac{1}{1 + 10^{(logIC_{50} - log\ \ ) \cdot h}}$$

Non-linear least square fits were solved by GraphPad Prism version 6.02 (GraphPad Software Inc., La Jolla, CA, USA). Data are expressed as means±SEM.

1.2 Prediction of arrhythmogenic risk by the ECG database

We evaluated the 26 benchmark drugs (Table) using the database. Drug concentration-dependent changes in ECGs and corresponding locations in the multi-dimensional space are shown for each drug in Supplementary Figures 2.4 to 2.29.

1.3 Predictive ability of ECG indices for arrhythmogenic risk

We applied a multiple regression analysis to ECG indices, i.e., QT interval, T_{peak}-T_{end} and J-T_{peak}, with the extent of block of ionic currents as predictor variables using the following model,

$$Y = a_{\mathrm{INa}} \cdot x_{INa} + a_{\mathrm{IKs}} \cdot x_{IKs} + a_{\mathrm{IKr}} \cdot x_{IKr} + a_{\mathrm{ICa}} \cdot x_{ICa} + a_{\mathrm{INa,L}} \cdot x_{INa,L}$$

where Y = ΔQT, ΔJ − T_{peak}, or ΔT_{peak} −T_{end}, and x_{INa}, x_{IKs}, x_{IKr}, x_{ICa} and $x_{INa,L}$ are the extent of block of INa, IKs, IKr, ICa and INa,L, respectively.

However, because the occurrence of arrhythmia is expressed by a dichotomous variable (y), we applied a logistic regression analysis using the following model,

$$\mathrm{logit(p)} = \log\left[\frac{y}{(1-y)}\right] = \mathrm{P}$$

$$P = b_{\mathrm{INa}} \cdot x_{INa} + b_{\mathrm{IKs}} \cdot x_{IKs} + b_{\mathrm{IKr}} \cdot x_{IKr} + b_{\mathrm{ICa}} \cdot x_{ICa} + b_{\mathrm{INa,L}} \cdot x_{INa,L} + b_{int}$$

where x_{INa}, x_{IKs}, x_{IKr}, x_{ICa} and $x_{INa,L}$ are the extent of block of INa, IKs, IKr, ICa and INa,L, respectively. P indicates how close each combinatorial state is to the region of arrhythmia; thus, it may be an index of arrhythmia risk.

Parameter estimations were performed using R Statistical Software (Free Software Foundation Inc. MA, USA).

2. Verification of the partial differential equation solver

2.1 *Method*

Software code for the partial differential equation (PDE) solver used in this study was verified by two approaches. First, we solved the problem with known analytical solutions to evaluate exact errors and the convergence rate proposed by Pathmanathan and Gray (Pathmanathan & Gray, 2014). Among the various benchmark tests provided in the literature, the three-dimensional (3D) bi-domain-with-bath problem (BB-3D*) conforms to the current heart simulation model, including the torso. As these authors pointed out, however, it is essentially a one-dimensional problem. Accordingly, we solved both BB-3D* and simple 3D bi-domain (B-3D) problems. The tissue domain ($\Omega = [0,1] \times [0,1] \times [0,1]$) for B-3D is a cube, and that for BB-3D* is flanked by two cubic bath domains ($\Omega_b = [-1,0] \times [0,1] \times [0,1]$ or $[1,2] \times [0,1] \times [0,1]$) of the same size (SFig. 1.4A). At all points in Ω, the extracellular ($\emptyset_e$) and intracellular ($\emptyset_i$) potentials and the membrane potential $V = \emptyset_i - \emptyset_e$ are defined. The governing equations in Ω are

$$\chi\left(C_m \frac{\partial V}{\partial t} + I_{ion}(\boldsymbol{u}, V)\right) - \nabla \cdot \left(\sigma_i \nabla (V + \emptyset_e)\right) = I_i^{stim}$$

$$\nabla \cdot ((\sigma_i + \sigma_e)\nabla \emptyset_e + \sigma_i \nabla V) = 0$$

$$\frac{\partial \boldsymbol{u}}{\partial t} = \boldsymbol{f}(\boldsymbol{u}, V)$$

where C_m is the capacitance of the cell membrane; χ is the membrane surface area-to-volume ratio; σ_i and σ_e are intracellular and extracellular conductivity tensors, respectively; I_i^{stim} is the stimulus current; $u \equiv u(\mathrm{t}, x)$ is the vector of state variables at time t and location x; I_{ion} is the ionic current calculated by the cell electrophysiology model. The following non-physiological cell model giving the analytical solution was used:

$$\boldsymbol{f}(\boldsymbol{u}, V) = \begin{bmatrix} (u1 + u2 - V)^2 u_2^2 + \frac{1}{2}(u_1 + u_3 - V)u_2^2(V - u_3) \\ -(u_1 + u_3 - V)u_2^3 \\ 0 \end{bmatrix}$$

$$I_{ion}(\boldsymbol{u}, V) = -\frac{C_m}{2}(u_1 + u_3 - V)u_2^2(V - u_3) + \frac{\beta(V - u_3)}{\chi}.$$

The bath domain satisfies

$$\nabla \cdot (s_b \nabla \emptyset_e) = 0.$$

Boundary conditions are continuity of extracellular potential $\emptyset_e$ and extracellular current across the boundary $\partial\Omega$. Also, a stimulus current applied to the edge of the bath domain (I_E^{surf}) must fulfill the following conditions:

$$\mathrm{n} \cdot (\sigma_b \nabla \emptyset_e) = I_E^{surf}$$

In the simple 3D bi-domain problem (B-3D), let $\mathrm{F}(\boldsymbol{x}) = \cos(\pi\mathrm{x})\cos(2\pi\mathrm{y})\cos(3\pi\mathrm{z})$ and $\mathrm{G}(\boldsymbol{x}) = 1 + \mathrm{x}y^2z^3$. We solved it with $I_i^{stim} = 0$ with a zero flux boundary condition and initial conditions $\mathrm{V}(0,\mathrm{x}) = \mathrm{F}(\mathrm{x})$ and $\mathrm{u}(0,\mathrm{x} = \big(\mathrm{G}(\mathrm{x}) + \mathrm{F}(\mathrm{x}), \mathrm{G}(x)^{-1/2}, 0\big)$ using the following parameter values.

$$\chi = 3, \qquad C_m = 2, \qquad \sigma_i = \pi^{-2}\begin{bmatrix} 1.1 & 0 & 0 \\ 0 & 1.2 & 0 \\ 0 & 0 & 0.3 \end{bmatrix}, \qquad \mathrm{k} = \frac{1}{\sqrt{2}},$$

$$\sigma_e = (1-k)\frac{\sigma_i}{k}, \quad \beta = -8.6(1-\mathrm{k}).$$

The exact solution in the unit cube $\Omega = [0,1] \times [0,1] \times [0,1]$ is

$$\mathrm{V}(\mathrm{t}, \boldsymbol{x}) = (1+t)^{\frac{1}{2}}F(\boldsymbol{x})$$

$$C(t) = k(1+t)^{\frac{1}{2}}$$

$$u_1(t, \boldsymbol{x}) = (1+\boldsymbol{x})G(\boldsymbol{x}) + (1+t)^{\frac{1}{2}}F(\boldsymbol{x})$$

$$u_2(t, \boldsymbol{x}) = (1+t)^{-1}(\mathrm{G}(\mathrm{x}))^{-\frac{1}{2}}$$

$$u_3(t, \boldsymbol{x}) = 0$$

For the 3D bi-domain-with-bath problem (BB-3D*), we applied an electrode stimulus of

$$I_E^{surf} = \begin{cases} \alpha \ \ if\ x = 2 \\ 0 \ \ otherwise \end{cases}$$

with $I_i^{stim} = 0$ and Dirichlet boundary condition applied $\emptyset_e = 0\ on\ x = -1$. Let $\mathrm{F}(\boldsymbol{x}) = \cos(\pi\mathrm{x})$ and $\mathrm{G}(\boldsymbol{x}) = 1 + \mathrm{x}y^2z^3$. With the initial conditions $\mathrm{V}(0,\mathrm{x}) = \mathrm{F}(\mathrm{x}) - ax/s_e$ and $\mathrm{u}(0,\mathrm{x} = \big(\mathrm{G}(\mathrm{x}) + \mathrm{F}(\mathrm{x}), \mathrm{G}(x)^{-1/2}, -ax/s_e\big)$, the following parameter values were used.

$$\chi = 3, \qquad C_m = 2, \qquad \sigma_i = \pi^{-2}\begin{bmatrix} 1.1 & 0 & 0 \\ 0 & 1.2 & 0 \\ 0 & 0 & 0.3 \end{bmatrix}, \qquad \mathrm{k} = \frac{1}{\sqrt{2}},$$

$$\sigma_e = (1-k)\frac{\sigma_i}{k}, \qquad \alpha = 0.01, \qquad s_b = \frac{s_e}{2}, \qquad \beta = -1.1(1-\mathrm{k}).$$

The exact solution in $\Omega_{\mathrm{all}} = [-1,2] \times [0,1] \times [0,1]$ is as follows.

$$\mathrm{V}(\mathrm{t},\boldsymbol{x}) = (1+t)^{\frac{1}{2}}F(\boldsymbol{x}) - \frac{\alpha}{s_e}\boldsymbol{x}$$

$$C(t) = k(1+t)^{\frac{1}{2}} + \frac{\alpha}{s_b}$$

$$\emptyset_e(t,\boldsymbol{x}) = \begin{cases} -k(1+t)^{\frac{1}{2}} + \frac{\alpha}{s_b} + C(t) & if\ -1 \le x \le 0 \\ -k(1+t)^{\frac{1}{2}}\cos(\pi x) + \frac{\alpha}{s_e}x + C(t) & if\ 0 \le x \le 1 \\ -k(1+t)^{\frac{1}{2}}\cos(\pi) + \frac{\alpha}{s_e} + \frac{\alpha}{s_b}(x-1) + C(t) & if\ 1 \le x \le 2 \end{cases}$$

$$u_1(t,\boldsymbol{x}) = (1+\boldsymbol{x})G(\boldsymbol{x}) + (1+t)^{\frac{1}{2}}F(\boldsymbol{x})$$

$$u_2(t,\boldsymbol{x}) = (1+t)^{-1}(\mathrm{G(x)})^{-\frac{1}{2}}$$

$$u_3(t,\boldsymbol{x}) = -\frac{\alpha}{s_e}x$$

We solved the problem using our PDE solver at four spatial resolutions ($h = 0.0125$, 0.025, 005, and 0.1). The results at t=1 were compared with the exact solution, and convergence was evaluated by calculating the standard L^2 and Sobolev H^1 spatial norms. For each spatial resolution (h), we adopted a different time step (Δt=0.00015625, 0.000625, 0.0025, and 0.01), so the time steps were proportional to h^2.

Second, we verified the code using the N-version strategy, wherein results from multiple simulation codes of a reproducible benchmark problem are used as a gold standard solution for the verification (Niederer et al., 2011). The following mono-domain equation is solved with this benchmark test

$$\chi\left(C_m\frac{\partial V}{\partial t} + I_{ion}(\boldsymbol{u},V)\right) = \nabla\cdot(\sigma\nabla V)$$

$$I_{ion} = f(y,t,V)$$

$$\frac{\partial \boldsymbol{y}}{\partial t} = g(y,t,V),$$

where C_m is the capacitance of the cell membrane; χ is the membrane surface area-to-volume ratio; σ is the conductivity; and I_{ion} is the ionic current calculated by a function (f) of a set of state variables (y) defined by a system of non-linear ordinary differential equations (g).

The ten Tusscher and Panfilov model of human epicardial myocytes (Ten Tusscher & Panfilov, 2006) is used for this benchmark test. The tissue model is a cuboid with dimensions of

3×7×20 mm. In this model, fiber direction is oriented in the long (20 mm) axis, and transversely isotropic conductivity is introduced. A zero-flux boundary condition is imposed, and the stimulus current is applied to a volume of 1.5×1.5×1.5 mm located at one corner of the cuboid (S in SFig 1.4B). The problem was solved at three spatial resolutions ($\Delta x = 0.5, 0.2, \text{and } 0.1$ mm), and each spatial resolution was solved with three time steps ($\Delta t = 0.05, 0.01, \text{and } 0.005$ ms). The definition of the model used for the benchmark test, model parameters, and the initial state variables of the cell model are listed in STables 1.2, 1.3, and 1.4, respectively. The time that the membrane potential passes through 0 mV upon first activation was used as the metrics of the model's behavior.

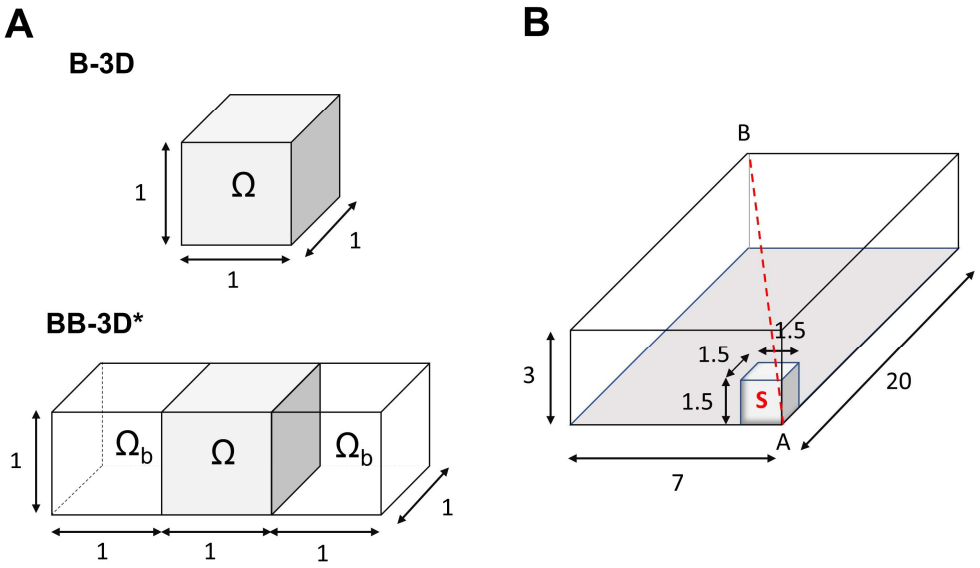

SFig. 1.4 Tissue models used for verification. A: *Top*: Model used for the B-3D problem, Ω: tissue domain. *Bottom*: Model used for the BB-3D* problem, Ω: tissue domain; Ω_b: bath domain. Numbers next to the double-headed arrow indicate size (in mm). **B**: Tissue model used for the N-version strategy. S: subdomain for application of stimulation. Numbers next to the double-headed arrow indicate size (in mm).

STable 1.4 Definition of the model used for the N-version benchmark test

Variable	Description
Equations	Mono-domain
Material	Transversely isotropic
PDE solver	Fully explicit
Cell model, variant	Ten Tusscher & Panfilov, 2006; epicardial cell model
Cell model numerical integration scheme	Explicit
Mesh type	Hexahedral
Solution method	Finite element
Basis function	Bi-linear
Pre-conditioners	Incomplete LU
Matrix solver	Generalized minimal residual
System architecture	Distributed memory

PDE: partial differential equation; LU: Lower-Upper

STable 1.5 Model parameters for the N-version benchmark test

Variables	Description
Geometric domain	Cuboid
Dimensions	20×7×3 mm
Fiber orientation	Fibers are aligned in the long (20 mm) axis
Discretization	0.5, 0.2, and 0.1 mm isotropic
PDE time steps	0.05, 0.01, and 0.005 ms
Stimulation geometry	1.5×1.5×1.5 mm cube from a corner
Stimulation protocol	2 ms at 50,000 μA cm^{-3}
Surface area-to-volume ratio	1400 cm^{-1}
Membrane capacitance	1 μFcm^{-2}
Conductivities: intra-longitudinal, intra-transversal, extra-longitudinal, and extra-transversal	0.17, 0.019, 0.62, and 0.24 Sm^{-1}

Table 1.6 Initial state variables of the cell model for the N-version benchmark test

Variable	Values (units)
Membrane potential	-85.23 (mV)
Rapid time-dependent potassium current Xr1 gate	0.00621
Rapid time-dependent potassium current Xr2 gate	0.4712
Slow time-dependent potassium current Xs gate	0.0095
Fast sodium current m gate	0.00172
Fast sodium current h gate	0.7444
Fast sodium current j gate	0.7045
L-type Ca current d gate	3.373×10^{-5}
L-type Ca current f gate	0.7888
L-type Ca current f2 gate	0.9755
L-type Ca current fClass gate	0.9953
Transient outward current s gate	0.999998
Transient outward current r gate	2.42×10^{-8}
Intracellular calcium	0.000126 (mM)
Sarcoplasmic reticulum calcium	3.64 (mM)
Subspace calcium	0.00036 (mM)
Ryanodine receptor R prime	0.9073
Intracellular sodium	8.604 (mM)
Intracellular potassium	136.89 (mM)

2.2 *Results*

SFigure 1.5A compares the distributions of membrane potential (V, left) and extracellular potential ($\emptyset_e$, right) at the end time (T=1) calculated by our solver (FE analysis): spatial resolution = 0.2 mm) with the exact solution for the B-3D problem. Simulation results well reproduce the exact solutions. Furthermore, errors of the membrane potential (SFig. 1.5B, left) and extracellular potential (SFig. 1.5B, right) evaluated by the Sobolev H^1 spatial norm (red line) and L^2 spatial norm (black line) decreased monotonically with mesh size. The slopes of the log–log plot were 1 and 2, respectively. The magnitudes of errors were also within the range reported in Figure 3 of Pathmanathan and Gray (Pathmanathan & Gray, 2014). Similarly good agreements in potential distribution and convergence were obtained for the BB-3D* problem **(SFig. 1.6)**. As for N-version verification, we plotted the local activation time along the line in the test domain (red broken line in SFig. 1.4B) simulated using three spatial resolutions: 0.1 mm (red line), 0.2 mm (green line), 0.5 mm (blue line) **(SFig. 1.7A)**. The velocity of the activation wave (reciprocal of the slope) increased with the refinement of meshes and converged at lower spatial resolutions. Similar patterns can be seen in 9 of 11 simulations reported in Figure 2 of Niderer et al. (Niederer et al., 2011). The activation time at the end was also similar (~50 ms). We plotted this activation time in SFig. 1.7B as a function of both time steps and spatial resolution. The activation time is less dependent on the time step and, in the region $\Delta x \leq 0.2$ mm and $\Delta t \leq 0.1$ ms, we confirmed convergence. Again, similar results have been reported for 9 of 11 program codes in Figure 3 of Niderer et al. (Niederer et al., 2011).

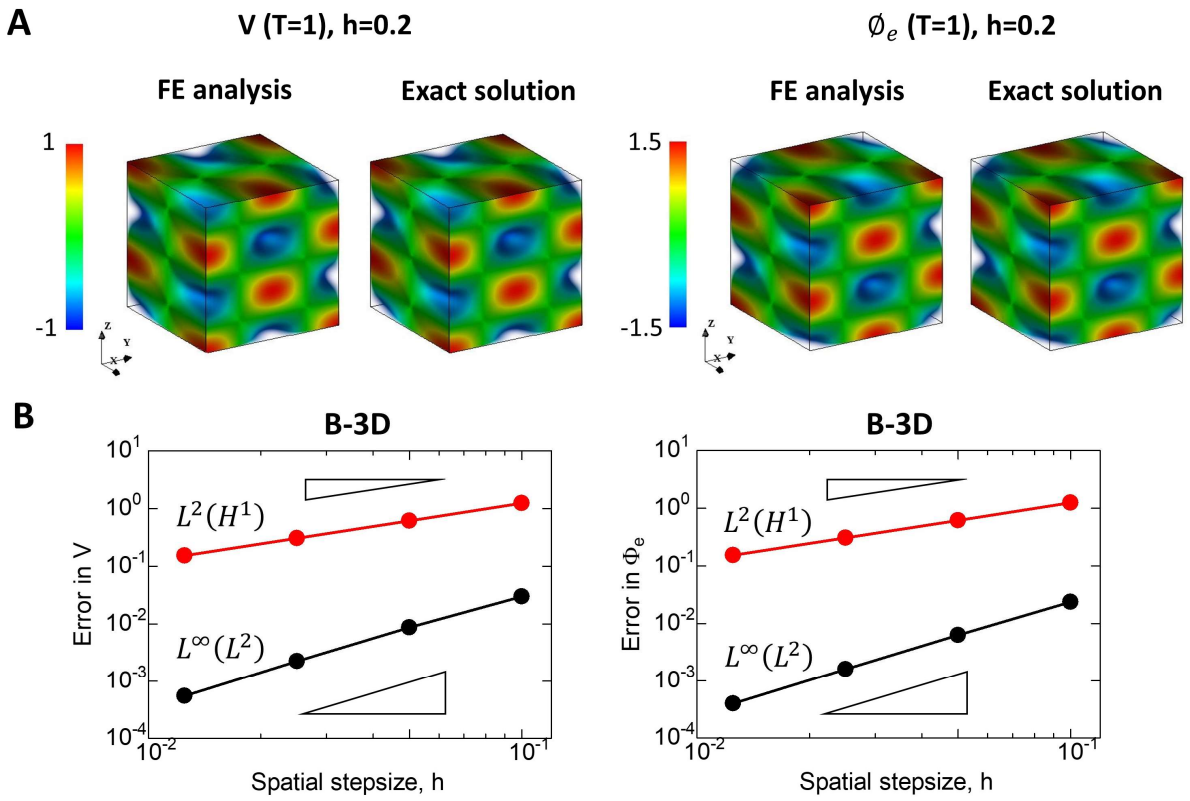

SFig. 1.5 Verification using the B 3D problem. A: Distribution of the membrane potential (V: *left*) and extracellular potential ($\emptyset_e$: *right*) at the end time (T=1) were compared between simulation results (FE analysis) and exact solutions. **B:** Errors in membrane potential (V: *left*) and extracellular potential ($\emptyset_e$: *right*) evaluated by the L^2 spatial norm (red line) and the Soblev H^1 spatial norm (black line) are plotted as functions of the spatial resolution.

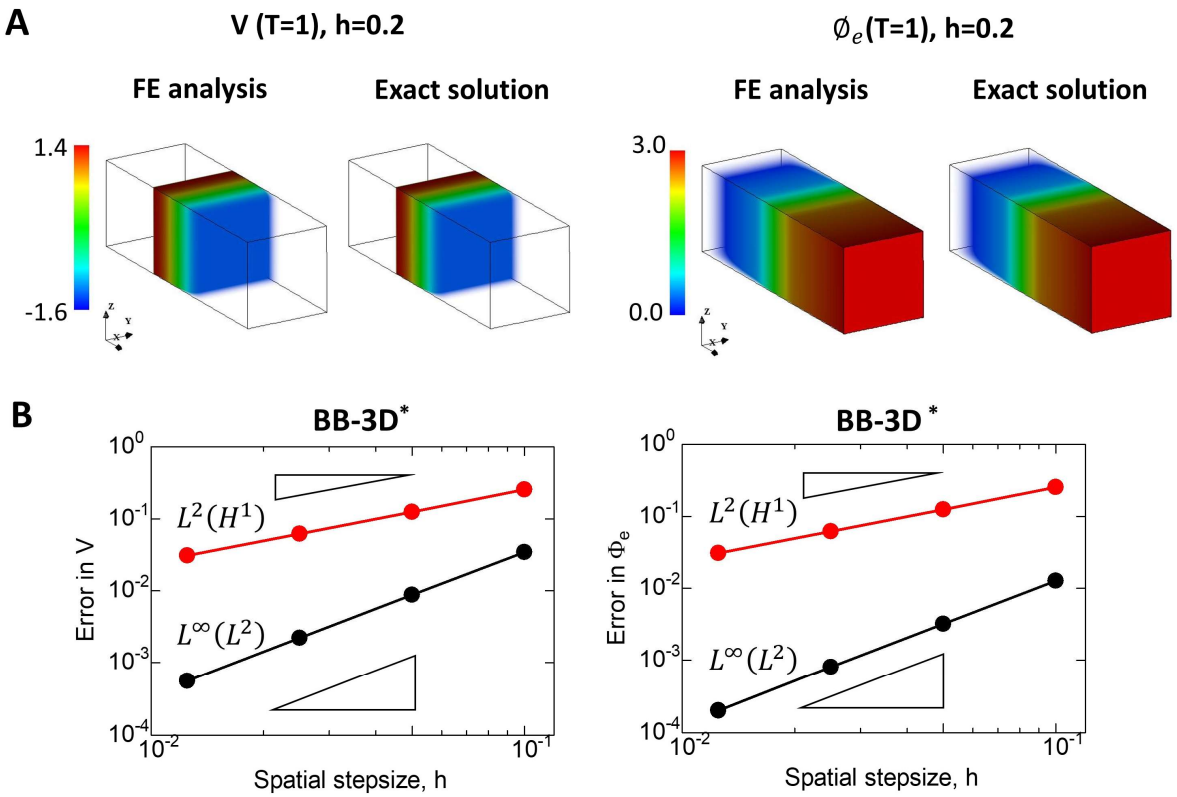

SFig. 1.6 Verification using the BB 3D* problem. A: Distribution of the membrane potential (V: *left*) and extracellular potential ($\emptyset_e$: *right*) at the end time (T=1) were compared between simulation results (FE analysis) and exact solutions. **B:** Errors in the membrane potential (V: *left)* and extracellular potential ($\emptyset_e$: *right*) evaluated by the L^2 spatial norm (red line) and Soblev H^1 spatial norm (black line) are plotted as functions of the spatial resolution.

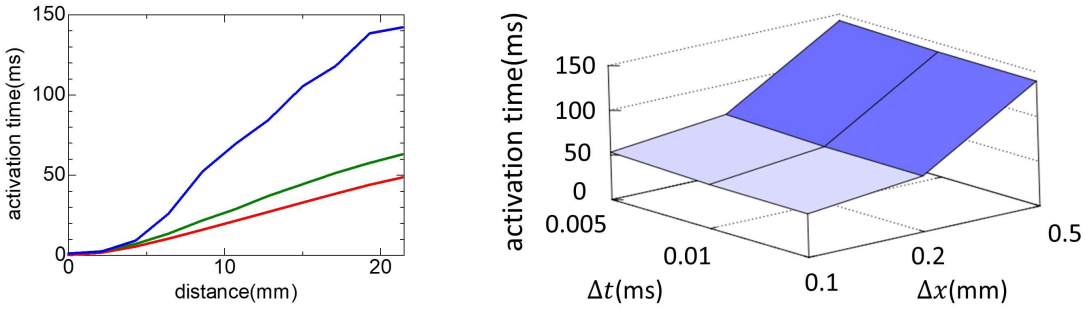

SFig. 1.7 Verification using the N-version strategy. A: Local activation times simulated with three spatial resolutions (Δx = 0.5 mm, blue line; 0.2 mm, green line; 0.1 mm, red line) are plotted as a function of the distance from the stimulation point. **B:** Activation time at the end point was simulated using different time steps and spatial resolutions.

References

Camacho MA, Lehr L, & Eisenberg SR (1995). A three-dimensional finite element model of human transthoracic defibrillation: paddle placement and size. IEEE Transactions on Biomedical Engineering 42**:** 572-578.

De Ambroggi L, Taccardi B, & Macchi E (1976). Body-surface maps of heart potentials: tentative localization of pre-excited areas in forty-two Wolff-Parkinson-White patients. Circulation 54**:** 251-263.

Durrer D, van Dam RT, Freud GE, Janse MJ, Meijler FL, & Arzbaecher RC (1970). Total excitation of the isolated human heart. Circulation 41**:** 899–912.

Keldermann RH, ten Tusscher KHWJ, Nash MP, Bradley CP, Hren R, Taggart P*, et al.* (2009). A computational study of mother rotor VF in the human ventricles. Am J Physiol 296**:**H370-H379.

Niederer SA, Kerfoot E, Benson AP, Bernabeu MO, Bernus O, Bradley C*, et al.* (2011). Verification of cardiac tissue electrophysiology simulators using an N-version benchmark. Phil Trans R Soc A 369**:** 4331-4351.

O'Hara T, Virag L, Varro A, & Rudy Y (2011). Simulation of the undiseased human cardiac ventricular action potential: model formulation and experimental validation. PLoS Computational Biology 7**:** e1002061.

Okada J, Washio T, Maehara A, Momomura S, Sugiura S, & Hisada T (2011). Transmural and apicobasal gradients in repolarization contribute to T-wave genesis in human surface ECG. Am J Physiol 301**:** H200–208.

Okada J, Yoshinaga T, Kurokawa J, Washio T, Furukawa T, Sawada K*, et al.* (2015). Screening system for drug-induced arrhythmogenic risk combining a patch clamp and heart simulator. Science Advances 1.

Panescu D, Webster JG, Tompkins WJ, & Stratbucker RA (1995). Optimization of cardiac defibrillation by three-dimensional finite element modeling of the human thorax. IEEE Transactions on Biomedical Engineering 42**:** 185-192.

Pathmanathan P, & Gray RA (2014). Verification of computational models of cardiac electrophysiology. Int J Numer Meth Biomed Engng 30**:** 525-544.

Stewart P, Aslanidi OV, D. N, Noble PJ, Boyett MR, & Zhang H (2009). Mathematical models of the electrical action potential of Purkinje fibre cells. Philos Transact A Math Phys Eng Sci 367**:** 2225–2255.

Taccardi B (1966). Ventricular repolarization body surface distribution of equipotential lines during atrial depolarization and ventricular repolarization. Circ Res 19**:** 865-878.

Ten Tusscher KHWJ, Noble D, Noble PJ, & Panfilov AV (2004). A model for human ventricular tissue. Am J Physiol 286**:** H1573-H1589.

Ten Tusscher KHWJ, & Panfilov AV (2006). Alternans and spiral breakup in a human ventricular tissue model. Am J Physiol 291**:** H1088-H1100.